

CNN+FoF: application of deep learning to the identification of dark matter haloes

Soumadeep Maiti,^{1,2*} Carlos M. Correa,² Andrea Fiorilli,² Andrés N. Ruiz,^{3,4} Dante J. Paz,^{3,4}
Alejandro Pérez Fernández,² Ariel G. Sánchez^{1,2}

¹Ludwig-Maximilians-Universität München, Geschwister-Scholl-Platz 1 80539 München, Germany

²Max Planck Institute for Extraterrestrial Physics, Giessenbachstr. 1, 85748 Garching, Germany

³Instituto de Astronomía Teórica y Experimental, UNC–CONICET, Laprida 854, X5000BGR Córdoba, Argentina

⁴Observatorio Astronómico, UNC, Laprida 854, X5000BGR Córdoba, Argentina

Accepted XXX. Received YYY; in original form ZZZ

ABSTRACT

We present a deep-learning-based approach for identifying dark matter haloes in cosmological N-body simulations. Our framework consists of a volumetric Convolutional Neural Network to classify individual simulation particles as either halo or non-halo members, followed by a highly optimised and parallelised Friends-of-Friends clustering algorithm that groups the classified halo members into distinct haloes. The training data comprise simulations generated using GADGET-4, with labels obtained with the ROCKSTAR halo finder. Our models incorporate two main halo mass definitions, M_{200b} and M_{vir} , with similar performance. For haloes defined by the ROCKSTAR M_{200b} criterion, the classification network demonstrated stable performance across multiple simulation resolutions. For the highest resolution, it achieved over 98% across all primary performance metrics when identifying halo particles. Furthermore, the FoF algorithm yielded halo catalogues with a purity generally exceeding 95% and a stable completeness of 93% for masses above $5 \times 10^{11} M_{\odot}$. Our pipeline recovered the centre-of-mass positions, velocities and halo masses with high fidelity, yielding a halo mass function consistent to within 5% of the reference while faithfully reconstructing the internal density profiles. The primary objective of this study is to offer a faster and scalable alternative to conventional halo finders, achieving a speed-up of approximately one order of magnitude relative to ROCKSTAR, offering a promising pathway for modern simulation-based inference methods that rely on rapid and accurate structure identification.

Key words: methods: numerical – methods: statistical – cosmology: large-scale structure of Universe

1 INTRODUCTION

The Lambda cold dark matter (ΛCDM) model is the standard theoretical framework for describing the gravitational evolution of the large-scale structure of the Universe from small initial density perturbations. Numerical N-body simulations based on this model show that gravitational instability drives the non-linear growth of these perturbations, giving rise to the cosmic web: a complex network of voids, filaments, and gravitationally bound structures (Peebles 1980; Bond et al. 1996). These virialised objects, known as dark matter haloes, are the fundamental nodes of the cosmic web, acting as the gravitational potential wells where baryonic matter accumulates to form galaxies, groups, and clusters (e.g., White & Rees 1978; White & Frenk 1991). The identification of these haloes in numerical simulations is therefore a central step in connecting theoretical predictions to observable galaxy and cluster populations.

A variety of algorithms have been developed to identify dark matter haloes in simulation outputs. The simplest approaches, such as the friends-of-friends (FoF, Davis et al. 1985) and spherical overdensity (SO, Warren et al. 1992; Lacey & Cole 1994; Hadzhiyska et al. 2022) techniques, locate haloes by tracing overdensities in the matter dis-

tribution. Grid-based schemes, such as Amiga’s Halo Finder (AHF, Knollmann & Knebe 2009), define the density field on an adaptive mesh and iteratively remove unbound particles to identify gravitationally bound structures. More sophisticated phase space algorithms such as ROCKSTAR (Behroozi et al. 2013), exploit both spatial and velocity information to identify haloes and substructures with high precision. These established tools are essential for constructing mock catalogues (e.g. Springel et al. 2005; Hernández-Aguayo et al. 2023; Euclid Collaboration et al. 2025), which are indispensable for interpreting galaxy surveys and provide critical input for testing and refining cosmological analysis pipelines.

Beyond their use in traditional model testing, the landscape of cosmological inference is undergoing a rapid transformation, placing new and stringent requirements on the entire pipeline used to generate synthetic galaxy samples that are compared against observations. Modern approaches, specifically field-level inference (Jasche & Lavaux 2019; Stadler et al. 2023; Nguyen et al. 2024) and simulation-based inference (SBI, e.g., Ishida et al. 2015; Alsing et al. 2018; Hahn et al. 2022; Tucci & Schmidt 2024), require forward models that are extremely fast and designed for massive, high-throughput execution. Machine learning methods, specially volumetric Convolutional Neural Networks (CNNs), have emerged to address this need. They have proven effective in cosmology due to their ability to learn hierarchi-

* E-mail: maitisoumadeep@gmail.com

cal representations from high-dimensional data. Applications have ranged from density field reconstruction (Chen et al. 2025) and direct parameter inference (Pan et al. 2020) to modelling non-linear structure formation (He et al. 2019; Jamieson et al. 2023). CNNs can dramatically accelerate the field generation step and are natively GPU-compatible. However, the step of identifying structures often relies on traditional, iterative, CPU-based halo finders, which become a severe computational bottleneck for these integrated, GPU-accelerated pipelines.

The application of machine learning to resolve such bottlenecks has evolved from simple feature-based classification to deep field-level emulation. For example, Lucie-Smith et al. (2022) used Random Forests to classify dark matter particles into halo/non-halo categories, demonstrating that local density information in the initial conditions is the primary driver of halo collapse, rendering tidal shear features largely redundant. The introduction of volumetric CNNs enabled the direct mapping of initial density fields to final halo catalogues. Berger & Stein (2019) employed a three-dimensional VNet architecture to segment proto-halo regions in the initial conditions (Lagrangian patches), while Bernardini et al. (2020) extended this approach by decoupling the task into classification and regression networks to better capture the scatter in the halo-mass relation. This task has also been addressed using differentiable frameworks that solve the inverse problem, namely, reconstructing the initial conditions (Modi et al. 2018; Charnock et al. 2020). The state-of-the-art has further expanded to include fully differentiable halo mass function predictions that propagate gradients to cosmological parameters (Buisman et al. 2025) and architectures that incorporate velocity field data to resolve non-linearities in high-variance regimes (Etezad-Razavi et al. 2025).

While the aforementioned methods focus largely on the initial conditions or on approximate predictions, our goal is to explore the feasibility of detecting virialised haloes directly from the fully evolved, non-linear particle distribution, capturing the full complexity of gravitational collapse. Inspired by the deep learning strategies of Berger & Stein (2019) and the architectural design of He et al. (2019), we employ a GPU-native VNet architecture to perform binary classification at the particle level. The network uses particle positions and velocities as input to assign a halo-membership probability to every simulation particle. A highly optimised and parallelised, CPU-based FoF algorithm is then applied exclusively to the predicted halo members in order to partition them into individual objects. This hybrid ‘‘CNN+FoF’’ pipeline offers a pathway to integrate halo identification directly into GPU-accelerated emulation frameworks. By using the CNN to prune the search space and identify candidate halo members on the GPU, the subsequent clustering task is significantly reduced, since the bulk of the particle classification is performed in a single forward pass. This allows the hybrid pipeline to remain compatible with the massive throughput requirements of next-generation inference techniques.

This paper is organised as follows. In Section 2, we describe the methodology used to generate the training samples from cosmological N-body simulations, including the extraction of particle features and the labelling procedure required for supervised learning. Section 3.1 introduces the architecture employed for binary classification, designed to predict whether individual dark matter particles belong to a halo or not. We also outline the training procedure and optimisation strategy adopted to achieve an accurate classification. Section 3.2 presents our approach to grouping the filtered particles into distinct objects and recovering halo centres, based on the application of a highly optimised and parallelised FoF clustering algorithm to the particles classified as halo members. Using this method, we reconstruct halo catalogues and evaluate their consistency with the

Table 1. Cosmological parameters of the N-body simulations used in our analysis. We assume a flat Λ CDM cosmological model. We list the physical baryon and cold dark matter densities, ω_b , ω_c , the dimensionless Hubble parameter, h , and the amplitude and spectral index of the primordial scalar mode, A_s and n_s .

Parameter	Value
ω_b	0.02244
ω_c	0.1206
h	0.67
n_s	0.96
A_s	2.1×10^{-9}

Table 2. Dark matter particle mass, m_p , for the different resolution configurations used in this work. Each configuration is specified by its box size L in Mpc, and the total number of dark matter particles, N .

Configuration	$m_p [M_\odot]$
$L200 - N32^3$	4.3498×10^{12}
$L200 - N64^3$	5.4372×10^{11}
$L200 - N128^3$	6.7965×10^{10}
$L100 - N128^3$	8.4957×10^9

expected halo distributions. In Section 4, we analyse the performance of the complete pipeline. We begin by evaluating the CNN model and assessing its predictive accuracy. We then examine the recovered halo properties, with particular emphasis on the halo mass function, complemented by an internal structural analysis of the catalogue objects, in order to assess their agreement with the testing sample. Finally, Section 5 summarises our findings and outlines potential directions for future improvements.

2 SIMULATION DATA SET

In this Section, we describe the generation and preparation of the cosmological N-body simulation data used for model training and analysis, including the procedure for assigning binary labels to individual dark matter particles.

We generated a suite of cosmological N-body simulations using the publicly available code GADGET-4 (Springel et al. 2021), assuming a flat Λ CDM cosmology at redshift $z = 0$. The cosmological parameters used for all simulations are listed in Table 1. The initial conditions were generated at a starting redshift of $z_{IC} = 99$ from a uniform cubic grid using the 2LPTIC code (Crocco et al. 2006, 2012).

We considered four simulation configurations to span a range of box sizes and resolutions: $L200-N32^3$, $L200-N64^3$, $L200-N128^3$, and a high-resolution configuration, $L100-N128^3$ ¹. Here, L denotes the simulation box length in Mpc and N refers to the total number of dark matter particles. Higher resolutions provide finer spatial sampling of the non-linear matter field, enabling better characterisation of the internal structure of dark matter haloes. The resulting mass per dark matter particle, m_p , for the different configurations is summarised in Table 2. Unless otherwise stated, we refer throughout this work to the highest resolution configuration, as all resolutions exhibit similar results.

We identified gravitationally bound structures in these simulations using the ROCKSTAR halo finder (Behroozi et al. 2013), which is recognized for its high accuracy in phase space. The haloes were

¹ The actual box size is 93.75 Mpc, chosen to match the resolution of the AletheiaEmu simulation suite of Sanchez et al. (2025) and Fiorilli et al. (2025).

defined using two different overdensity-based mass definitions: M_{vir} and M_{200b} . The subscript 'b' indicates multiples of the comoving background matter density, ρ_b , while the virial mass overdensity threshold was defined by the fitting formula given by [Bryan & Norman \(1998\)](#) for flat cosmologies. These definitions corresponded to the radii r_{vir} and r_{200b} , respectively, which defined the spherical boundary of the halo.

To generate the ground-truth labels for our supervised learning task, a particle was labeled as a halo member ($y = 1$) if it was identified as gravitationally bound and lay within the overdensity radius of any halo found by ROCKSTAR. All remaining particles were labeled as non-halo particles ($y = 0$). We restricted our final halo catalogues to objects containing 25 or more member particles to ensure that the identified haloes are numerically stable, avoiding poorly resolved transient overdensities dominated by sampling noise.

For each resolution, the full simulation suite was randomly divided into three subsets for training, validation, and testing. The training set comprised 350 simulations, providing a broad sampling of structural diversity. The validation set contained 50 simulations, employed to monitor convergence and prevent overfitting, while the test set included 100 simulations and served as an independent benchmark for performance assessment. Each resolution thus had its own triplet of datasets, maintaining a uniform and reproducible framework for model comparison.

3 HYBRID HALO-FINDING PIPELINE

3.1 CNN for binary classification

Our particle classification network is based on the three-dimensional version of the VNet architecture implemented in the D^3M framework of [He et al. \(2019\)](#), which was developed to reproduce the non-linear evolution of cosmological density fields in N-body simulations. The D^3M model extends the classical UNet design of ([Ronneberger et al. 2015](#)) to three dimensions and operates intrinsically at the particle level, learning a one-to-one mapping between input and output voxels corresponding to individual simulation particles. This formulation preserves the physical correspondence between each particle and its predicted quantities.

We adapted the D^3M framework to perform voxel-wise binary classification, where each voxel retains its correspondence with a single simulation particle. In this formulation, the network infers, for every particle, the probability of being a halo member. The architecture follows a standard encoder–decoder layout with skip connections, allowing simultaneous recovery of large-scale structural context and fine-scale spatial features that are essential for accurate halo identification. The details of the final configuration are shown in [Table 3](#).

The encoder (contracting path) comprises three downsampling stages, each containing two $3 \times 3 \times 3$ convolutional layers with stride 1 and periodic padding, which preserve spatial dimensions while increasing the number of feature maps, followed by a stride-2 convolution that performs spatial downsampling. The number of channels doubles at each level, from 64 to 128 and then 256, enabling the model to capture progressively coarser and more complex representations of the density field. The decoder (expanding path) mirrors this structure, using transposed convolutions for upsampling followed by two standard convolutional layers at each level. Skip connections concatenate feature maps from the encoder to their corresponding decoder layers, ensuring that fine spatial details are retained and that gradients flow efficiently during training. All intermediate layers employ ReLU activations and batch normalisation to enhance convergence stability and mitigate internal covariate shift.

Table 3. Summary of our CNN architecture for particle classification.

Parameter	Value
Input Channels	6 (displacement + velocity)
Output Channels	1 (halo probability)
Architecture Depth	3 downsampling + 3 upsampling levels
Conv3D Layers per Level	2
Initial Filters	64
Maximum Filters	256
Activation Functions	ReLU (intermediate), Sigmoid (final)
Loss Function	BCE
Optimizer	Adam (lr = 0.001)
Input Shape	$N_{\text{res}} \times N_{\text{res}} \times N_{\text{res}} \times 6$
Output Shape	$N_{\text{res}} \times N_{\text{res}} \times N_{\text{res}} \times 1$
Trainable Parameters	$\sim 8.4 \times 10^6$

To adapt the architecture for binary classification, the final layer of the decoder is modified to produce a single output channel per voxel, followed by a sigmoid activation function:

$$\phi(x) = \frac{1}{1 + e^{-x}}. \quad (1)$$

This non-linear function maps each raw output x to a probability in the range $[0, 1]$, representing the likelihood that a given particle belongs to a dark matter halo. While the sigmoid activation is widely used in binary classification due to its probabilistic output, it is also susceptible to vanishing gradients in very deep networks. Nonetheless, for our architecture depth, it provides a suitable mechanism for assigning soft binary labels.

The initial Lagrangian particle distribution is embedded into a regular three-dimensional lattice in which each voxel contains exactly one simulation particle. The input to the network is therefore represented as a six-channel voxelised tensor that encodes both spatial and dynamical information for each simulation particle. Each voxel contains the three Cartesian components of the displacement field, $\Psi = (\Psi_x, \Psi_y, \Psi_z)$, representing deviations from the initial grid positions, together with the three components of the velocity vector, $v = (v_x, v_y, v_z)$, describing the particle velocities.

The complete input volume is therefore structured as

$$X \in \mathbb{R}^{N_{\text{res}} \times N_{\text{res}} \times N_{\text{res}} \times 6}, \quad (2)$$

where N_{res} denotes the resolution of the simulation along one dimension (i.e., $N = N_{\text{res}}^3$ represents the total number of particles). This ensures a one-to-one correspondence between the input of the network and the individual simulation particles. This combination of displacement and velocity information allows the network to effectively infer the signature of gravitationally bound structures from both the positional and dynamical configuration of the matter field.

The final output of the network is a single-channel tensor of the form

$$Y \in \mathbb{R}^{N_{\text{res}} \times N_{\text{res}} \times N_{\text{res}} \times 1}, \quad (3)$$

in which each voxel contains a scalar probability score that can be thresholded or interpreted directly to determine halo membership.

The model was trained in a supervised fashion using ground-truth labels derived from the ROCKSTAR halo catalogue as described in [Section 2](#). The network was optimised using the binary cross-entropy (BCE) loss function,

$$\mathcal{L}_{\text{BCE}} = -[y \log(\hat{y}) + (1 - y) \log(1 - \hat{y})], \quad (4)$$

where $y \in \{0, 1\}$ denotes the ground-truth label and \hat{y} is the predicted probability from the network output. This formulation is standard for binary classification tasks with probabilistic predictions ([Goodfellow 2016](#)). Optimisation was performed using the Adam algorithm

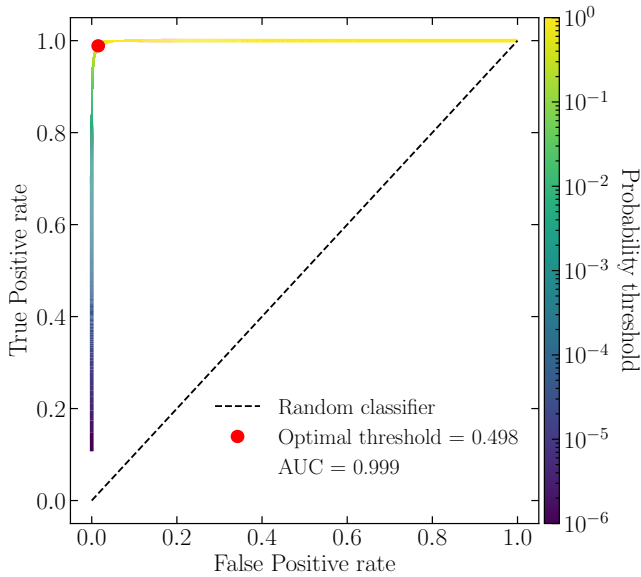


Figure 1. ROC curve showing the CNN’s ability to distinguish halo and non-halo particles across varying probability thresholds. The red point indicates the best threshold for the classification, corresponding to $y = 0.498$.

(Kingma & Ba 2014) with default parameters and a fixed learning rate of 10^{-3} . Random shuffling was applied across mini-batches of 3D volumes to improve generalisation, and early stopping based on validation loss was employed to prevent overfitting.

We set a maximum training duration of 120 epochs, determined empirically to ensure full convergence while maintaining computational efficiency. Additional runs confirmed that the validation loss consistently reached its minimum before this limit (typically between 50 and 110 epochs), indicating that convergence was achieved well before the upper bound. The model weights corresponding to the epoch with the minimum validation loss were stored, providing an empirical estimate of the best-performing model for each resolution.

The full training pipeline was implemented in Python using the PyTorch deep-learning framework (Paszke et al. 2019). Multi-GPU parallelisation was achieved through the `nn.DataParallel` module, which enabled the use of large batch sizes and substantially reduced training time. All models were trained on the high-performance Raven GPU cluster at the Max Planck Computing and Data Facility (MPCDF²), taking advantage of the high throughput of NVIDIA A100 GPUs for tensor operations.

3.2 FoF algorithm to group distinct haloes

As described in the previous section, the CNN step identifies particles that belong to haloes. However, it does not associate these particles with individual halo clumps. For the particular redshift and cosmology considered here, this classification step dramatically reduces the set of particles that must be further considered to roughly 37% of the total number of particles. While this percentage is specific to the $L100-N128^3$ simulation and varies slightly with resolution, the resulting data is inherently clumpy, as the predicted halo particles occupy localised regions in space separated by large empty areas.

² <https://www.mpcdf.mpg.de>

Table 4. Confusion matrix of the CNN particle classification for the high-resolution $L100 - N128^3$ configuration. Values represent the percentage of the total particle population falling into each category: true positives (TP), false positives (FP), true negatives (TN), and false negatives (FN).

True Class	Predicted Class	
	Halo	Non-Halo
Halo	36.25% (TP)	0.71% (FN)
Non-Halo	0.60% (FP)	62.44% (TN)

This structure is the key element that enables the optimisation of the subsequent halo-finding step.

To identify the individual haloes and their particle memberships, we run a classic FoF algorithm, which computes pairwise particle distances and assigns the same halo membership to particles whose separation is below a given linking length, λ . This threshold length is typically defined as a small fraction of the mean interparticle separation; in our case, we used $\lambda = 0.17 \bar{n}^{-1/3}$, where \bar{n} is the mean particle number density. The grouping process is transitive, resembling a breadth-first search (BFS) on a graph where nodes are particles connected by edges shorter than the linking length.

Since traditional FoF algorithms based on direct particle searches are inherently serial, their efficient parallelisation on concurrent computing systems is complex. Our FoF approach exploits two facts: first, the input data are already highly clustered (thanks to the preceding CNN step) and naturally separated into distinct spatial domains. Second, we reduce the cost of pairwise distance calculations by implementing a grid technique.

For the second point, we divide the simulation box into regular cubic grids, or voxels, and reorder the input particle array along a Peano-Hilbert space-filling curve. This optimisation improves cache behaviour in the memory-demanding stages of computation. The voxel methods used here have proved highly efficient in other contexts, such as void finding algorithms, and we adopt the publicly available functions for voxel manipulation from the Popcorn void-finder code (Paz et al. 2023).

We run a two-stage FoF search. First, a voxel-level FoF search is performed. At each BFS stage, we identify, in parallel, every group of non-empty voxels whose minimum separation (the distance between the closest vertices) is below the linking length. Parallel efficiency is limited here by the need to prevent race conditions, forcing some execution parts to remain serial. The cost of this stage scales with the number of non-empty voxels rather than the total particle count. Second, after isolating these connected voxel groups, we carry out a particle-level FoF run, assigning each spatial domain to its own thread. This decomposition makes the workload embarrassingly parallel, eliminates race conditions in halo assignment, and allows us to significantly outperform traditional particle-based FoF finders. A final optimisation from the Popcorn library links particles in voxel pairs whose maximum separation is below the linking length in one step, removing many needless pairwise distance calculations.

Individual halo structures are identified by applying the optimised FoF clustering algorithm to the set of particles predicted as halo members by the CNN. This procedure groups the majority of particles into distinct haloes, for which we define the spatial centre as the centre of mass of the constituent particles. To ensure that the final catalogue is complete, any remaining particles—classified as halo members by the CNN but not linked to a group by the FoF—are subsequently assigned to their nearest identified halo centre. The total mass of each halo is then computed as the sum of the masses of its FoF-linked particles plus any assigned residual particles. This approach

Table 5. Performance metrics of the CNN particle classification for all the resolution configurations used in this work. The definitions of the metrics are provided in Appendix B.

Metric	$L200 - N32^3$	$L200 - N64^3$	$L200 - N128^3$	$L100 - N128^3$
Accuracy	0.99	0.98	0.98	0.99
Precision	0.96	0.95	0.97	0.98
Recall	0.96	0.96	0.97	0.98
Specificity	0.99	0.98	0.99	0.99
F1 Score	0.96	0.95	0.97	0.98
MCC	0.98	0.97	0.98	0.98
AUC	0.98	0.98	0.98	0.99
AP	0.93	0.95	0.95	0.99

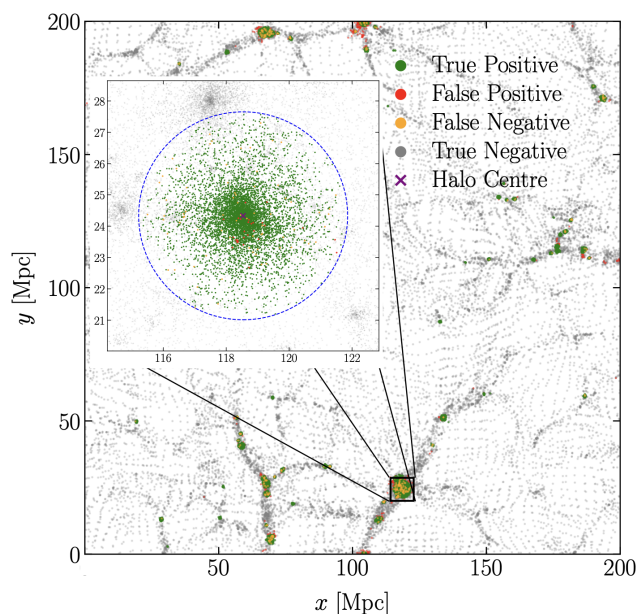


Figure 2. Spatial distribution of particles in one of the $L200-N128^3$ test simulations, colour-coded by classification category: true positives (green), false positives (red), false negatives (orange), and true negatives (grey). The main panel displays a projected slice (depth of 2.5% of the box size) illustrating the large-scale cosmic web. The inset zooms in on a representative halo identified by ROCKSTAR, with the centre marked by a purple cross and the r_{200b} radius indicated by a dashed blue circle. The network successfully traces the main halo body, while misclassifications are concentrated at the halo outskirts.

leverages the FoF algorithm to locate and deblend structures while ensuring every particle detected by the neural network contributes to the final mass budget.

4 RESULTS

In this section, we present the results of applying the hybrid CNN+FoF pipeline to the N -body simulation test set. We first focus on assessing the particle-level classification accuracy, and later on properties of the recovered haloes, comparing the statistical and structural properties of the final halo catalogue to the ROCKSTAR reference. We also compare the computational performance of our pipeline against a full ROCKSTAR run. While the results in this section adopt M_{200b} as the primary reference, the corresponding analysis

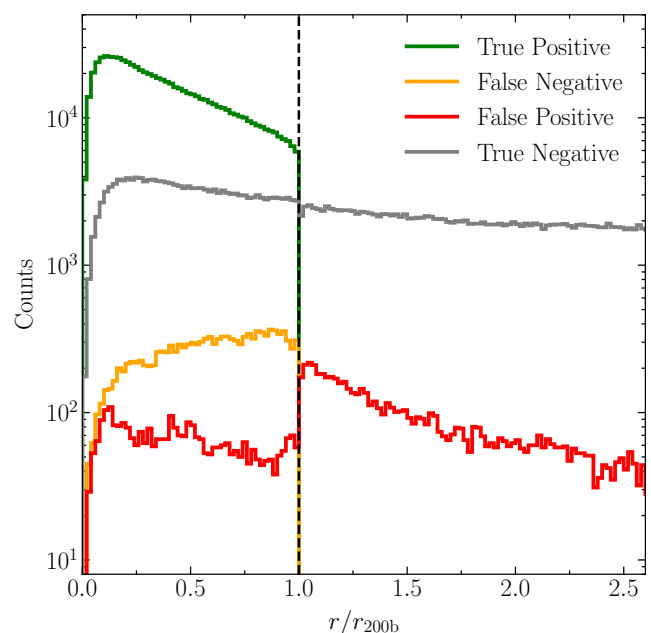


Figure 3. Normalised radial distribution of particles relative to the nearest ROCKSTAR halo centre, scaled by the r_{200b} radius. The vertical dashed line marks the halo boundary at $r = r_{200b}$. Inner regions are dominated by true positives (green), which decline at the halo radius, indicating accurate identification of gravitationally bound particles. Misclassifications (false negatives, orange; false positives, red) peak around the halo radius, reflecting the challenge of distinguishing particles located near the boundary. True negatives (grey) dominate the outer regions, although there is a significant fraction of them located inside r_{200b} . Histogram counts are shown on a logarithmic scale.

for M_{vir} is provided in Appendix A. Moreover, we focus the analysis mainly on the $L100-N128^3$ configuration, with the other cases leading to similar results.

4.1 Particle classification accuracy

To quantify the accuracy of the classification performed by our network into halo and non-halo particles, we categorise each particle-label prediction based on its agreement with the ground-truth labels from ROCKSTAR. Particles identified as halo members by both ROCKSTAR and the classification network are termed true positives (TP), while those classified as halo particles by the CNN but not by ROCKSTAR are defined as false positives (FP). Conversely, false

negatives (FN) correspond to particles that ROCKSTAR labels as halo members but the CNN predicts as non-halo. Finally, true negatives (TN) denote the particles consistently recognised as non-halo by both methods.

Figure 1 presents the receiver operating characteristic (ROC) curve corresponding to the high-resolution $L100-N128^3$ configuration, which traces the trade-off between the true positive rate and the false positive rate across varying classification thresholds. The red point marks the optimal threshold of $y = 0.498$, which we used for binary classification throughout our analysis.

Using this optimal threshold, the predicted probabilities are converted into binary labels and compared against the ground-truth labels. The resulting confusion matrix, detailing the fraction of particles in each category, is shown in Table 4.

The classification performance of the trained CNN is further evaluated using standard metrics computed on the test simulations, which are reported in Table 5 for all resolution configurations. Definitions and notation for all metrics are provided in Appendix B. For the highest resolution, the network attains an accuracy of 98.69%, with precision and recall values of 98.01% and 98.42%, and a specificity of 98.80%. These results demonstrate that the classifier effectively captures the primary halo features, maintaining a stable balance between precision and recall across the tested resolutions.

The spatial distribution of the classified particles provides further insight into the network’s predictive behaviour. Figure 2 presents a spatial visualisation of the classified particles in a projected slice of one of the $L200-N128^3$ simulations. TP particles (green) form compact, high-density clusters that align with gravitationally bound structures. TN particles (grey) dominate the underdense regions, confirming the network’s reliability in identifying the background field. Misclassified particles, FP (red) and FN (orange), are typically concentrated near the peripheries of haloes where density gradients are steep.

To quantify this effect, we computed the normalised radial distance, r/r_{200b} , between each particle and its closest ROCKSTAR halo centre. Figure 3 shows the distribution of the normalised radial distance r/r_{200b} for particles in the TP, FP, FN, and TN groups. Notice that the TP and FN distributions are confined within $r/r_{200b} \leq 1$ by definition. The TP distribution, on the one hand, shows a strong concentration towards the centre, consistent with the spherical overdensity criterion used to define halo membership and indicating correct identification of particles associated with halo centres. The FN distribution, on the other hand, peaks near $r/r_{200b} = 1$, indicating that incorrect halo assignments occur primarily in regions close to the halo boundary where the transition between halo and background particles occurs. A similar behaviour is observed for FP particles, which are also mostly located near $r/r_{200b} = 1$, reflecting the difficulty of classification in boundary regions where particle densities and binding properties vary. Unlike FN, FP particles can go beyond $r/r_{200b} = 1$, indicating that lower mass clumps were also identified by the CNN, although they do not qualify for ROCKSTAR requirements. Finally, TN particles follow a broad distribution, consistent with their association with the background field. Notice also that there are significant TN inside the boundary marked by $r = r_{200b}$. These distributions show that the classifier does not rely solely on radial distance but distinguishes halo membership based on learned phase space information. Overall, the radial distributions show that the network reproduces the spatial structure of haloes, with accurate classification in central regions and consistent behaviour near halo boundaries.

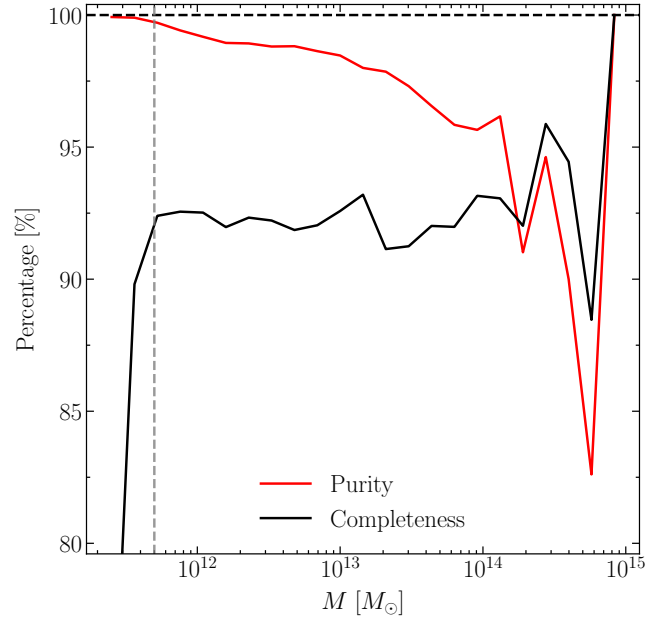


Figure 4. Mass-dependent purity (red) and completeness (black) of the CNN+FoF halo catalogue relative to the reference ROCKSTAR sample. The completeness exceeds 90% across a wide mass range, remaining stable at $\sim 93\%$ above $M = 5 \times 10^{11} M_{\odot}$ (grey vertical line). The drop at the low-mass arises as we approach the resolution limit. Conversely, the purity generally exceeds 95%, but exhibits a mass-dependent decline. This drop can be attributed to FoF fragmentation at lower masses and to the merging of adjacent structures at the high-mass end.

4.2 Recovering halo properties

After particle classification, the optimised FoF algorithm was applied to the predicted halo members to build the final halo catalogues. To evaluate the consistency and precision of the resulting catalogue, we calculated the distance between the centres of the FoF haloes and that of the nearest ROCKSTAR halo, d_{FR} . A match between both catalogues was defined as the cases in which this distance was less than the ROCKSTAR r_{200b} radius. In cases where multiple FoF haloes were found within this radius, only the nearest was retained.

To quantify the fidelity of the CNN+FoF catalogue relative to the ROCKSTAR reference, we evaluate two primary metrics: purity and completeness. Purity, P , measures the fraction of recovered haloes that are real (i.e., have a counterpart in the reference catalogue), while completeness, C , measures the fraction of reference haloes successfully recovered by our pipeline. Formally, we define these metrics as a function of halo mass, M :

$$P(M) = \frac{N_{\text{matched}}(M)}{N_{\text{CNN+FoF}}(M)},$$

$$C(M) = \frac{N_{\text{matched}}(M)}{N_{\text{ROCKSTAR}}(M)}. \quad (5)$$

Table 6 summarises the global values of these statistics (over the full mass range) for all resolution configurations. For the highest resolution, the pipeline achieves a global completeness of 89.34%, indicating that the vast majority of reference haloes are successfully recovered. The catalogue also exhibits high fidelity, with a global purity of 99.38%, corresponding to a low spurious detection rate.

While these global statistics demonstrate robust overall performance, the reconstruction quality varies with halo mass. Figure 4

Table 6. Global purity and completeness for the CNN+FoF halo catalogues across different resolutions. Purity is defined as the fraction of recovered haloes that have a counterpart in the reference ROCKSTAR catalogue, while completeness denotes the fraction of reference haloes successfully recovered by the pipeline.

Metric	$L200 - N32^3$	$L200 - N64^3$	$L200 - N128^3$	$L100 - N128^3$
Purity	97.79%	98.53%	99.18%	99.38%
Completeness	87.75%	87.19%	86.43%	89.34%

shows purity and completeness as functions of halo mass according to the definitions given in equation (5). The purity remains high across a broad mass range, generally exceeding 95%, although it exhibits a mass-dependent decline. We attribute the drop at the low-mass end to fragmentation by the FoF algorithm, which artificially classifies substructures as satellites around massive host haloes, while the decrease at the high-mass end is likely driven by the merging of adjacent structures. Overall, the reconstructed catalogue is largely representative of the underlying halo population, with minimal spurious detections in the lower- and intermediate-mass regimes. The completeness is similarly stable; it exceeds 90% across a wide mass range and remains constant at $\sim 93\%$ above $M = 5 \times 10^{11} M_\odot$. The expected decline at the low-mass end arises as we approach the resolution limit, where haloes are composed of fewer particles, leading to an increased sensitivity of these poorly sampled structures to boundary definitions. Based on these stability metrics, we adopt $M = 5 \times 10^{11} M_\odot$ as the lower mass limit for the remainder of the analyses in this work.

To evaluate the precision of the recovered halo properties, we compared the centre-of-mass (CM) positions and velocities of the matched haloes with those of the ROCKSTAR halo catalogue as a reference. For each matched pair, we computed the component-wise offsets $\Delta \mathbf{X} = \mathbf{X}^{\text{CNN+FoF}} - \mathbf{X}^{\text{ROCKSTAR}}$, and normalised them by the ROCKSTAR r_{200b} radius, yielding the dimensionless quantities $\Delta X_i/r_{200b}$, where $i \in \{x, y, z\}$. Similarly, for the velocities, we evaluated the component-wise ratios $V_i^{\text{ROCKSTAR}}/V_i^{\text{CNN+FoF}}$.

Figure 5 shows the resulting distributions for the normalised position offsets and velocities. The former are sharply peaked at zero and exhibit symmetric, narrow profiles across all three spatial components, indicating that halo centres are recovered to within a small fraction of the halo radius. The velocity ratios are correspondingly well centred around unity with modest scatter, demonstrating that the reconstructed haloes preserve the bulk kinematic properties of the ROCKSTAR reference catalogue. Together, these results confirm that the CNN+FoF pipeline recovers both the spatial and dynamical properties of haloes.

To further assess the performance of our pipeline, we compared the total masses of the recovered haloes with their corresponding values in the ROCKSTAR reference catalogue. This comparison is presented in Figure 6 as a density plot, which displays the average distribution of halo masses across the 100 test set simulations. The results show a tight linear correlation across the entire mass range, indicating that the combined CNN-classification and proximity-based particle assignment effectively captures the total mass of the underlying gravitational structures. At the low-mass end, we note a slight increase in the scatter. This is expected, as haloes in this regime consist of relatively few particles, making their mass estimates more sensitive to small variations in the CNN’s particle-level classification and the subsequent deblending by the FoF stage. However, even in this limit, the pipeline maintains high fidelity, as evidenced by the high purity and completeness metrics discussed previously. For higher-mass systems, the scatter reduces significantly, demonstrating the robustness of the method for the massive clusters that drive many large-scale structure statistics.

We now turn our attention to the halo mass function (HMF), a

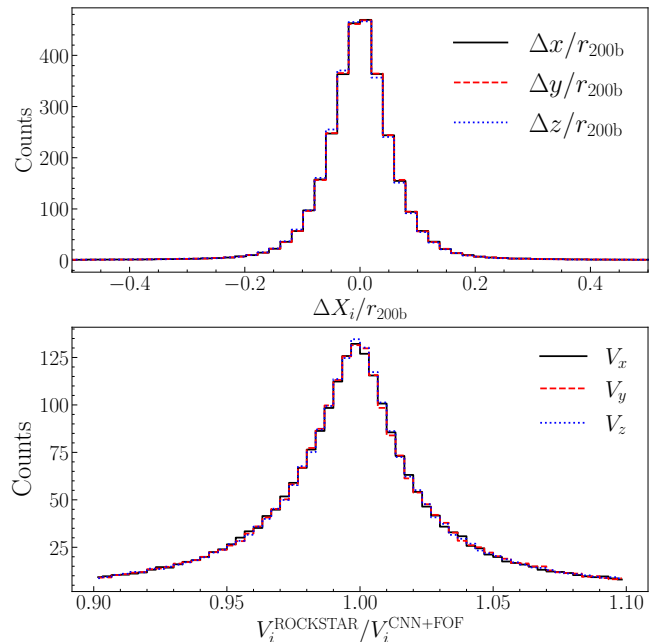


Figure 5. Accuracy of recovered halo properties for the matched CNN+FoF and ROCKSTAR samples. *Top:* Distribution of centre-of-mass position offsets, ΔX_i , normalised by the r_{200b} radius, along each Cartesian axis. *Bottom:* Distribution of the component-wise velocity ratios, $V_i^{\text{ROCKSTAR}}/V_i^{\text{CNN+FoF}}$. The position offsets are sharply peaked at zero, while the velocity ratios cluster tightly around unity, demonstrating that the pipeline recovers both the spatial and bulk dynamical properties of haloes with high fidelity.

fundamental cosmological statistic. While the previous comparison focused strictly on cross-matched pairs, the HMF requires the complete halo population; therefore, we compute it using the full samples, including the unmatched haloes discussed earlier. Figure 7 presents the comoving number density of haloes per logarithmic mass interval, $n(M) = dN/d \log M dV$, derived from both the CNN+FoF pipeline and the reference ROCKSTAR catalogues. We observe good consistency between the two, with deviations within 5% across the intermediate and high-mass ranges.

We conclude this section by analysing the recovered internal structure of the haloes. Using the full catalogues, we computed the spherically averaged mass density profiles, $\rho(r)$, for both the CNN+FoF and the reference ROCKSTAR catalogues. We divided the samples into five mass bins spanning the entire mass range considered in our work. The resulting comparisons are presented in Figure 8. The CNN+FoF profiles closely track the ROCKSTAR results across all mass ranges, demonstrating that our pipeline accurately recovers the detailed internal structure of the haloes.

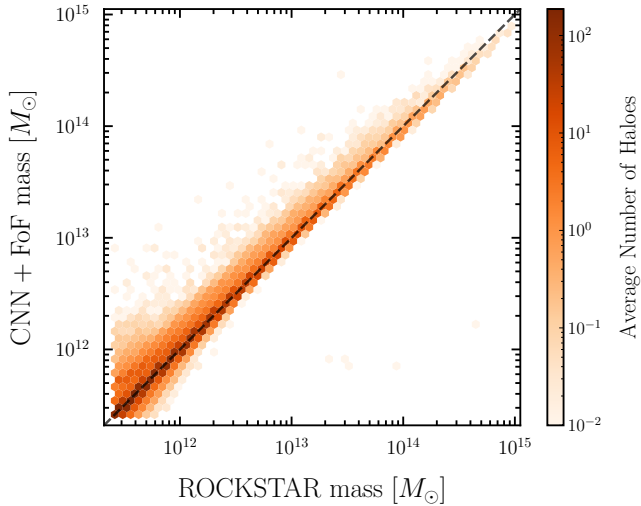


Figure 6. Comparison of the halo masses recovered by the hybrid CNN+FoF pipeline against the reference values from the ROCKSTAR catalogue. The hexagonal bins are colour-coded by the average number of haloes per bin. The dashed black line represents the 1:1 relation. The tight distribution along the diagonal across several orders of magnitude demonstrates the high fidelity of the mass recovery, with minimal systematic bias. The scatter at the low-mass end reflects the inherent difficulty in precisely defining boundaries for haloes composed of a limited number of particles.

4.3 Computational performance

To evaluate the computational speed-up achieved by our method, we compared the total execution time of the CNN+FoF pipeline against ROCKSTAR across multiple simulation resolutions.

Figure 9 shows the mean runtime for each method. The CNN+FoF pipeline achieves a consistent speed-up of approximately one order of magnitude relative to ROCKSTAR, with runtime ratios ranging from 8 to 12 across all tested resolutions. This improvement arises from the CNN’s ability to infer halo membership in a single, GPU-native forward pass, which is far faster than the iterative six-dimensional phase-space search dominating the cost in ROCKSTAR. The subsequent highly-optimised and parallelised, CPU-based FoF clustering step operates efficiently on the drastically reduced subset of particles classified as halo members, further enhancing overall performance.

We note that the current framework treats the classification (GPU-native) and FoF (CPU-based) stages as separate modules. The wall-clock time is dominated by input-output operations and the parallel FoF clustering step, rather than the CNN forward pass. Ongoing work aims to integrate the clustering operation directly within the neural network architecture, extending our CNN toward a fully end-to-end halo finder.

5 CONCLUSIONS AND FUTURE WORK

In this study, we have presented a machine-learning-based framework for the identification of dark matter haloes in cosmological simulations. Our methodology combines the strengths of 3D Convolutional Neural Networks with a highly and parallelised FoF algorithm to create a hybrid pipeline (CNN+FoF) capable of rapidly reconstructing halo catalogues from raw simulation data.

The classification network demonstrated stable performance across multiple simulation resolutions. For the highest-resolution

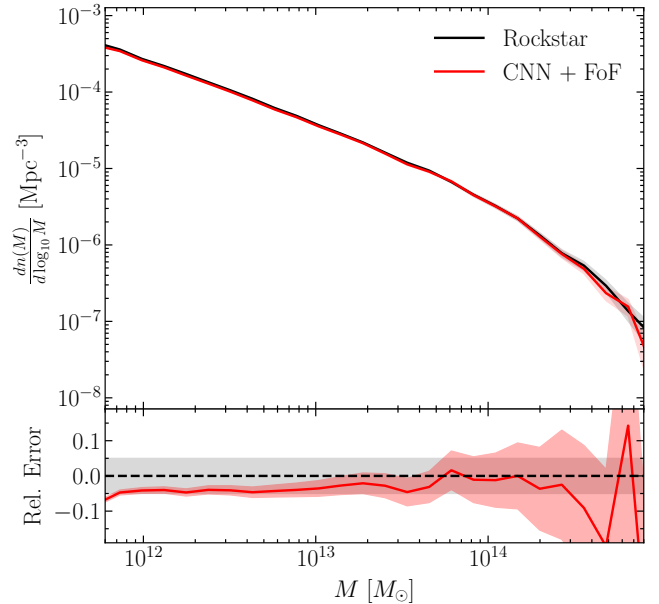


Figure 7. Comparison of the recovered halo mass function from the CNN+FoF pipeline (red) with the ROCKSTAR reference catalogue (black). The bottom panel shows the relative fractional deviation between the two estimates. The CNN+FoF reconstruction agrees within 5% across the majority of the mass range, with deviations emerging at low masses.

case, $L100 - N128^3$, the network consistently achieved over 98% across all primary performance metrics when distinguishing halo and non-halo particles. This particle-level classification served as a robust foundation for the subsequent halo identification. When grouped into individual objects, the resulting catalogue successfully matched 89.34% of the haloes identified by the ROCKSTAR phase-space finder. Spurious detections accounted for a negligible fraction (0.62%) of the total catalogue, indicating minimal contamination.

As a function of halo mass, the purity generally exceeds 95%, although it exhibits a mass-dependent decline attributed to FoF fragmentation at low masses and halo merging at the high-mass end. Completeness stabilises at approximately 93% above $5 \times 10^{11} M_{\odot}$, with a drop at the low-mass end arising as we approach the resolution limit. These results justify the adoption of $5 \times 10^{11} M_{\odot}$ as the lower mass limit for the analysis of halo properties.

The spatial and kinematic properties of the recovered haloes exhibited high fidelity relative to the reference catalogue. The normalised positional offsets, $\Delta X_i / r_{200b}$, were narrowly distributed around zero, and the component-wise velocity ratios were centred near unity with a small scatter.

The comparison of halo masses reveals that the CNN+FoF pipeline achieves good agreement with the ROCKSTAR ground truth. The recovered masses exhibited a tight linear correlation with the reference values, characterised by a mass-dependent scatter that significantly diminishes in the high-mass regime. This accuracy translates directly into a precise recovery of the halo mass function. When applying our method to the full catalogues, we reproduced the reference mass function with a consistency of better than 5% across intermediate and high masses.

Beyond global properties, our analysis confirms that the method accurately resolves the internal structure of dark matter haloes. We examined the spherically averaged density profiles, $\rho(r)$, and found that the CNN+FoF predictions closely track the ROCKSTAR results

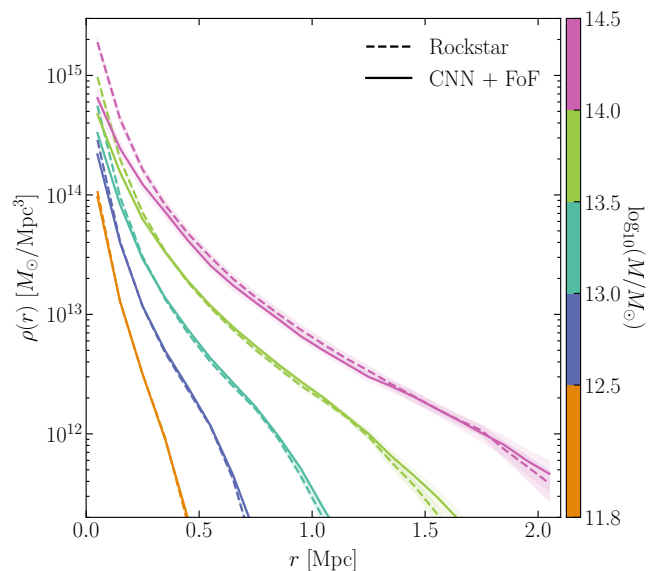


Figure 8. Mean spherically averaged density profiles of haloes identified by ROCKSTAR (dashed lines) and by the CNN+FoF pipeline (solid lines). Shaded regions indicate the standard deviation on the mean within each mass bin. The close agreement demonstrates that the CNN+FoF pipeline accurately reproduces the internal mass distribution of haloes.

across all mass ranges. This agreement demonstrates that our pipeline not only captures the total mass but also faithfully reconstructs the detailed matter distribution within the haloes.

Several avenues for further development remain. One immediate priority is the integration of the clustering stage directly into the neural network architecture. Replacing the current reliance on a CPU-based FoF step with a fully differentiable, end-to-end halo finder would further streamline the workflow and potentially increase throughput. Additionally, assessing the model’s performance across larger simulation volumes and varying cosmological parameters is essential to ensure its generalisability. In this context, techniques such as evolution mapping (Sánchez et al. 2022; Esposito et al. 2024; Sanchez et al. 2025; Fiorilli et al. 2025) could be leveraged to efficiently transfer learned features across different redshifts and cosmologies, significantly reducing the computational cost of training.

Ultimately, the primary value of this framework lies in its potential integration into next-generation cosmological analysis tools. By coupling this fast halo-finding pipeline with field-level emulators (e.g. He et al. 2019; Jamieson et al. 2023) and SBI frameworks, it becomes possible to construct unified and highly efficient forward modelling pipelines. In such frameworks, the rapid identification of haloes from emulated density fields enables the mass-production of mock catalogues necessary for likelihood-free inference, providing a scalable and efficient solution for the high-throughput requirements of modern cosmological surveys.

In summary, our study establishes a robust proof of concept that machine-learning-based halo identification can achieve comparable accuracy to traditional phase-space algorithms while delivering significant computational gains. By bridging the gap between deep learning and classical clustering methods, this hybrid approach provides an efficient alternative for halo identification, well-suited for the analysis of large-scale structure surveys.

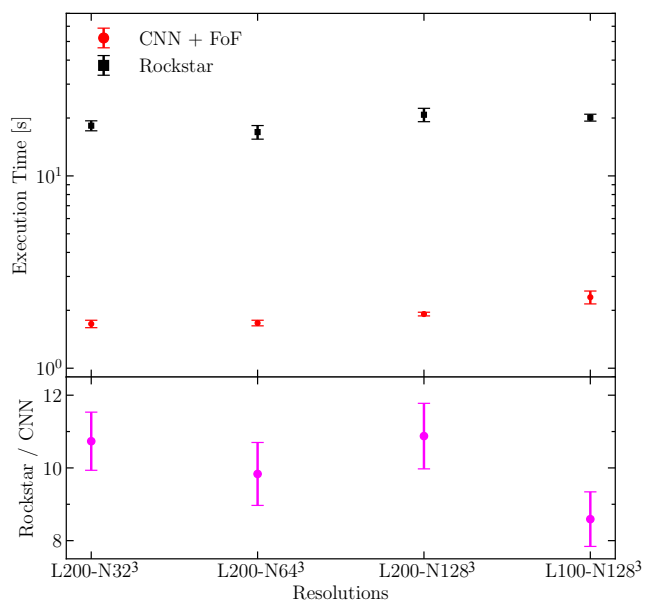


Figure 9. *Top:* wall-clock execution time of the CNN+FoF pipeline (red circles) and ROCKSTAR (black squares) measured across the different resolution configurations. *Bottom:* ratio of the ROCKSTAR to CNN+FoF run time. The CNN+FoF pipeline achieves a consistent speed-up of approximately one order of magnitude relative to ROCKSTAR.

ACKNOWLEDGEMENTS

We would like to thank Jiamin Hou and Sofia Contarini for their help and useful discussions. Special thanks to Matteo Esposito for his help sharing the tools to process our N-body simulations. This analysis was carried out on the HPC system Raven of the Max Planck Computing and Data Facility (MPCDF, <https://www.mpcdf.mpg.de>) in Garching, Germany. This work made extensive use of open-source scientific software, including PyTorch, NumPy, SciPy, Matplotlib, and pandas. This research was supported by the Excellence Cluster ORIGINS, which is funded by the Deutsche Forschungsgemeinschaft (DFG, German Research Foundation) under Germany’s Excellence Strategy - EXC-2094 - 390783311. CMC would like to specially thank Daniela Taborda and Martín Correa Taborda for their unconditional support.

DATA AVAILABILITY

The data underlying this article will be shared on reasonable request to the corresponding author.

REFERENCES

- Alsing J., Wandelt B., Feeney S., 2018, *MNRAS*, **477**, 2874
 Behroozi P. S., Wechsler R. H., Wu H.-Y., 2013, *ApJ*, **762**, 109
 Berger P., Stein G., 2019, *MNRAS*, **482**, 2861
 Bernardini M., Mayer L., Reed D., Feldmann R., 2020, *MNRAS*, **496**, 5116
 Bond J. R., Kofman L., Pogosyan D., 1996, *Nature*, **380**, 603
 Bryan G. L., Norman M. L., 1998, *ApJ*, **495**, 80
 Buisman J., List F., Hahn O., 2025, *arXiv e-prints*, p. [arXiv:2507.03074](https://arxiv.org/abs/2507.03074)
 Charnock T., Lavaux G., Wandelt B. D., Sarma Boruah S., Jasche J., Hudson M. J., 2020, *MNRAS*, **494**, 50

- Chen X., Padmanabhan N., Eisenstein D. J., 2025, *J. Cosmology Astropart. Phys.*, 2025, 055
- Crocce M., Pueblas S., Scoccimarro R., 2006, *MNRAS*, 373, 369
- Crocce M., Pueblas S., Scoccimarro R., 2012, 2LPTIC: 2nd-order Lagrangian Perturbation Theory Initial Conditions, Astrophysics Source Code Library, record ascl:1201.005 (ascl:1201.005)
- Davis M., Efstathiou G., Frenk C. S., White S. D. M., 1985, *ApJ*, 292, 371
- Esposito M., Sánchez A. G., Bel J., Ruiz A. N., 2024, *MNRAS*, 534, 3906
- Etezad-Razavi S., Abbasgholinejad E., Sotoudeh M.-H., Hassani F., Raesi S., Baghran S., 2025, *Phys. Rev. D*, 111, 043521
- Euclid Collaboration et al., 2025, *A&A*, 697, A5
- Fiorilli A., Ruiz A. N., Sanchez A. G., Esposito M., 2025, *arXiv e-prints*, p. arXiv:2511.16730
- Goodfellow I., 2016, Deep learning
- Hadzhiyska B., Eisenstein D., Bose S., Garrison L. H., Maksimova N., 2022, *MNRAS*, 509, 501
- Hahn C., et al., 2022, *arXiv e-prints*, p. arXiv:2211.00723
- He S., Li Y., Feng Y., Ho S., Ravanbakhsh S., Chen W., Póczos B., 2019, *Proceedings of the National Academy of Science*, 116, 13825
- Hernández-Aguayo C., et al., 2023, *MNRAS*, 524, 2556
- Ishida E. E. O., et al., 2015, *Astronomy and Computing*, 13, 1
- Jamieson D., Li Y., de Oliveira R. A., Villaescusa-Navarro F., Ho S., Spergel D. N., 2023, *ApJ*, 952, 145
- Jasche J., Lavaux G., 2019, *A&A*, 625, A64
- Kingma D. P., Ba J., 2014, *arXiv e-prints*, p. arXiv:1412.6980
- Knollmann S. R., Knebe A., 2009, *ApJS*, 182, 608
- Lacey C., Cole S., 1994, *MNRAS*, 271, 676
- Lucie-Smith L., Peiris H. V., Pontzen A., Nord B., Thiyagalangam J., Piras D., 2022, *Phys. Rev. D*, 105, 103533
- Modi C., Feng Y., Seljak U., 2018, *J. Cosmology Astropart. Phys.*, 2018, 028
- Nguyen N.-M., Schmidt F., Tucci B., Reinecke M., Kostić A., 2024, *Phys. Rev. Lett.*, 133, 221006
- Pan S., Liu M., Forero-Romero J., Sabiu C. G., Li Z., Miao H., Li X.-D., 2020, *Science China Physics, Mechanics, and Astronomy*, 63, 110412
- Paszke A., et al., 2019, *arXiv e-prints*, p. arXiv:1912.01703
- Paz D. J., Correa C. M., Gualpa S. R., Ruiz A. N., Bederián C. S., Graña R. D., Padilla N. D., 2023, *MNRAS*, 522, 2553
- Peebles P. J. E., 1980, *The large-scale structure of the universe*. Princeton University Press.
- Ronneberger O., Fischer P., Brox T., 2015, *arXiv e-prints*, p. arXiv:1505.04597
- Sánchez A. G., Ruiz A. N., Jara J. G., Padilla N. D., 2022, *MNRAS*, 514, 5673
- Sanchez A. G., et al., 2025, *arXiv e-prints*, p. arXiv:2511.13826
- Springel V., et al., 2005, *Nature*, 435, 629
- Springel V., Pakmor R., Zier O., Reinecke M., 2021, *MNRAS*, 506, 2871
- Stadler J., Schmidt F., Reinecke M., 2023, *J. Cosmology Astropart. Phys.*, 2023, 069
- Tucci B., Schmidt F., 2024, *J. Cosmology Astropart. Phys.*, 2024, 063
- Warren M. S., Quinn P. J., Salmon J. K., Zurek W. H., 1992, *ApJ*, 399, 405
- White S. D. M., Frenk C. S., 1991, *ApJ*, 379, 52
- White S. D. M., Rees M. J., 1978, *MNRAS*, 183, 341

APPENDIX A: PERFORMANCE WITH THE M_{vir} MASS DEFINITION

Previously, we presented the results corresponding to the halo definition based on M_{200b} for the L100–N128³ high-resolution simulation. Here, we report the analogous results obtained using the virial mass, M_{vir} , as a reference.

The classification results for M_{vir} are found to be highly consistent with those obtained for M_{200b} , indicating that the trained model generalises well across different mass definitions. The confusion matrix for this case is presented in Table A1, while Table A2 lists the corresponding performance metrics, including accuracy, precision, recall, and specificity. The values demonstrate that the classification

Table A1. Confusion matrix for the classification results using the virial mass definition, M_{vir} .

True Class	Predicted Class	
	Halo	Non-Halo
Halo	23.40% (TP)	0.87% (FN)
Non-Halo	0.89% (FP)	75.20% (TN)

Table A2. Performance metrics for the classification results using M_{vir} .

Metric	Value
Accuracy	0.98
Precision	0.96
Recall	0.96
Specificity	0.99
F1 Score	0.96
MCC	0.95

Table A3. Global purity and completeness statistics for the CNN+FoF halo catalogues using M_{vir} .

Metric	Value
Purity	99.18%
Completeness	86.43%

network maintains high performance, confirming its robustness with respect to variations in halo boundary criteria.

The halo matching statistics between the reconstructed catalogue and the ROCKSTAR reference catalogue are summarized in Table A3. The high matched fraction and low number of unmatched detections confirm the physical consistency of the reconstructed haloes and the reliability of the model when applied to virial mass definitions.

Overall, the consistent behaviour for the two mass definitions, M_{200b} and M_{vir} , demonstrates that the model effectively captures the fundamental physical correlations characterising gravitationally bound structures. Minor variations arise naturally from the different boundary definitions, yet the core predictive capability of the CNN remains robust across all conventions.

APPENDIX B: CONFUSION MATRIX AND DERIVED METRICS

To quantitatively evaluate the classification performance of our network, we employ standard metrics derived from the confusion matrix. Let TP, FP, TN, and FN denote the numbers of true positives, false positives, true negatives, and false negatives, respectively. These represent the counts of correctly and incorrectly classified particles relative to the ground-truth halo catalogue. The total number of positive and negative samples are $P = TP + FN$ and $N = TN + FP$, respectively, and $T = P + N$ denotes the total number of classified samples. With this nomenclature, the different metrics are defined as follows:

$$\text{Accuracy} = \frac{\text{TP} + \text{TN}}{T}, \quad (\text{B1})$$

$$\text{Precision} = \frac{\text{TP}}{\text{TP} + \text{FP}}, \quad (\text{B2})$$

$$\text{Recall (TPR)} = \frac{\text{TP}}{\text{TP} + \text{FN}}, \quad (\text{B3})$$

$$\text{Specificity (TNR)} = \frac{\text{TN}}{\text{TN} + \text{FP}}, \quad (\text{B4})$$

$$\text{F1} = \frac{2 \text{Precision} \times \text{Recall}}{\text{Precision} + \text{Recall}} = \frac{2 \text{TP}}{2 \text{TP} + \text{FP} + \text{FN}}, \quad (\text{B5})$$

$$\text{MCC} = \frac{\text{TP} \cdot \text{TN} - \text{FP} \cdot \text{FN}}{\sqrt{(\text{TP} + \text{FP})(\text{TP} + \text{FN})(\text{TN} + \text{FP})(\text{TN} + \text{FN})}}. \quad (\text{B6})$$

Accuracy measures the overall fraction of correctly classified particles, but it can be misleading when the data are imbalanced, as is often the case between halo and non-halo particles. Precision quantifies how many of the particles predicted as halo members actually belong to haloes in the reference catalogue, thus penalising false detections. Recall (or true positive rate) measures the completeness, i.e., the fraction of genuine halo particles recovered by the model. Specificity (true negative rate) complements recall by quantifying the fraction of background particles correctly recognised as non-halo. The F1 score provides a harmonic mean between precision and recall, balancing the trade-off between purity and completeness. Finally, the Matthews correlation coefficient (MCC) condenses the four confusion-matrix terms into a single balanced measure, remaining robust even for highly imbalanced datasets.

In addition to these threshold-dependent quantities, we compute threshold-independent metrics by sweeping the decision threshold $\tau \in [0, 1]$ across the sigmoid outputs. The area under the ROC curve (AUC) represents the probability that a randomly chosen positive sample is ranked higher than a randomly chosen negative one, serving as an overall measure of separability. The average precision (AP) is the integral of the precision–recall curve, summarising the trade-off between purity and completeness across all thresholds.

In our application, high precision corresponds to few spurious detections (i.e., minimising FP particles), while high recall indicates that the majority of true halo particles are recovered. Metrics such as F1 and MCC, therefore, provide a compact way to assess the balance between purity and completeness of the resulting classification. Scalar metrics in Table 5 are reported at the best classification threshold τ , while AUC and AP summarise the global classification performance across all thresholds.

This paper has been typeset from a $\text{\TeX}/\text{\LaTeX}$ file prepared by the author.